

Enhanced Lithiation Cycle Stability of ALD-Coated Confined a-Si Microstructures Determined Using In Situ AFM

Collin R. Becker,*† S.M. Prokes,‡ and Corey T. Love§

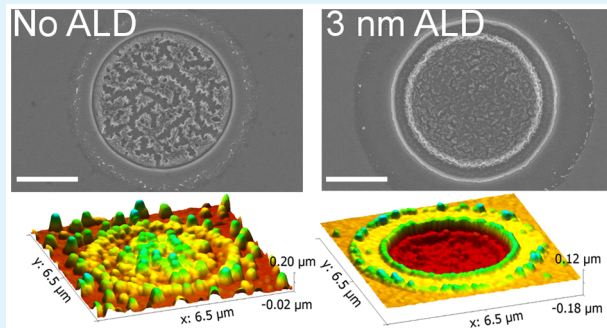
†Electrochemistry Branch, US Army Research Laboratory, 2800 Powder Mill Road, Adelphi, Maryland 20783, United States

‡Electronic Science & Technology Division, US Naval Research Laboratory, Washington, DC 20375, United States

§Chemistry Division, US Naval Research Laboratory, Washington, DC 20375, United States

Supporting Information

ABSTRACT: Microfabricated amorphous silicon (a-Si) pits ~4 μm in diameter and 100 nm thick were fabricated to be partially confined in a nickel (Ni) current collector. Corresponding unconfined pillars were also fabricated. The samples were coated with 1.5, 3, or 6 nm of Al_2O_3 ALD. These samples were tested in electrolytes of 3:7 by weight ethylene carbonate:ethyl methyl carbonate (EC:EMC) with 1.2 M LiPF_6 salt with and without 2% fluoroethylene carbonate (FEC) and in a pure FEC electrolyte with 10 wt % LiPF_6 . The samples were imaged with an atomic force microscope during electrochemical cycling to evaluate morphology evolution and solid electrolyte interphase (SEI) formation. The partially confined a-Si structures had superior cycle efficiency relative to the unconfined a-Si pillars. Additionally, samples with 3 nm of ALD achieved higher charge capacity and enhanced cycle life compared to samples without ALD, demonstrated thinner SEI formation, and after 10 cycles at a 1 C rate remained mostly intact and had actually decreased in diameter. Finally, the samples with 3 nm of ALD had better capacity retention in the baseline 3:7 EC:EMC than in either of the FEC containing electrolytes.



KEYWORDS: silicon, lithium ion, atomic force microscopy, in situ, battery

1. INTRODUCTION

One of the most promising technologies for lightweight, portable, and efficient electrical energy storage is the lithium ion (Li-ion) battery.¹ State of the art Li-ion batteries make use of a lithium (Li) containing cathode material and a graphite anode that can store the Li ions between graphite sheets. One way to increase the energy density of the Li-ion battery is to replace the graphite anode with an alloy-type anode such as silicon, aluminum, germanium, or tin.^{2–8} These materials alloy with the Li^+ from the electrolyte, and Li^+ is replenished by the Li-containing cathode material to maintain electroneutrality. In the case of silicon (Si) about ten times more Li can be stored compared to traditional graphite anodes.⁵

During the alloy reaction a massive volume expansion up to 400% occurs, and as the Li is alloyed and dealloyed the silicon material crumbles. Whether the Si is particles, thin films, or single crystal form, this leads to rapid capacity fade as the broken particles lose connection with the current collector. Additionally, the fresh cleaved surfaces of the broken particles must be passivated by decomposing the electrolyte to form a solid electrolyte interphase (SEI). This process consumes Li^+ from the electrolyte and leads to further capacity loss.

To mitigate capacity loss and improve cycling efficiency, modifications to the Si electrode material, the electrolyte, and

SEI are under investigation. Electrolyte additives such as fluoroethylene carbonate (FEC) and vinylene carbonate (VC) have demonstrated promising performance gains.^{9,10} Also, intentionally mechanically constraining the expansion of the electrode materials improves Coulombic efficiency and reduces capacity fade.¹¹ Finally, surface coatings on the Si electrode of various oxides and polymers may create a better SEI than that which is formed under conventional battery cycling.^{12,13}

Atomic layer deposition (ALD) is a technology that is self-limiting; conformal; allows the precise control of the film thickness; and is capable of depositing ultrathin layers of metal oxide, polymer, or metal.¹⁴ A very thin ALD layer of only a few nanometers has shown benefits for corrosion protection, nanothermites, biomedical compatibility, and microelectronics use.^{15–19} Additionally, the extremely thin coatings can accommodate enormous strain.²⁰ For Li-ion batteries, the ALD coatings have been used on both anodes and cathodes on particles and in full electrodes with binders and conductive additives.^{21–23} The films show improved performance of batteries including capacity, kinetics, and efficiency.²⁴ Even on

Received: October 8, 2015

Accepted: December 16, 2015

Published: December 16, 2015

Si and other alloy type anodes with extreme volume expansion, ALD films have demonstrated improvements.^{25–27}

Aside from TEM studies using solid state electrolytes, few studies have investigated *in situ* behaviors of ALD films on anode materials.^{12,13,28,29} Recent work has demonstrated the utility of *in situ* AFM to not only study Li-ion batteries both for qualitative information regarding volume change, cracking, and SEI formation but also to quantitatively record properties such as elastic modulus and hardness.^{30–32} Scanning probe studies provide complementary information to *in situ* TEM where solid state electrolytes are typically employed and *in situ* XRD that uses conventional electrolytes but lacks morphological information.^{33,34}

In this work, FEC additive, mechanical confinement, and ALD are investigated to improve performance of a-Si electrodes. Specifically, aluminum oxide (Al_2O_3) is applied to thin film Si structures that are either semiconfined pits in a metal current collector or free to expand as pillars except on the bottom surface. The electrolytes include lithium hexafluorophosphate (LiPF_6) salt in ethylene carbonate (EC) and ethyl methyl carbonate (EMC) solvents with and without FEC additive. The structures are lithiated and delithiated in an electrochemical cell accessed by an AFM in a glovebox to monitor morphological changes of the structures. The AFM is also used ex-situ in electrical sensing mode to probe the stability of the ALD film pre- and postcycling.

2. EXPERIMENTAL SECTION

2.1. Microfabrication. A (100) oriented 1–5 Ω cm Si wafer is used as the handle wafer for fabrication of the anode structures. The 400 nm thick Ni current collector is deposited using an Evatek BAK 641 electron beam evaporator with a Veeco Mark II ion source that helps create a smooth Ni film. The deposition rate is 0.2 nm/s. The photoresist used for creating the electrode pattern is Microchem 5214 image reversal photoresist and is hardbaked (Axcelis Fusion 200) prior to ion milling.

Following photoresist patterning, the wafers are ion milled (4wave Instruments) to erode away the Ni film in patterned regions where the photoresist has been removed. The milling is accomplished in two etch steps, one at 95° for 370 s and one at 140° for 50 s. The etch time was chosen to mill at least 200 nm into the substrate but not cross into the Si handle wafer.

The 100 nm thick a-Si is also deposited from the Evatek BAK 641 and a 20 nm Ni adhesion layer is deposited prior to the a-Si deposition.

2.2. Atomic Layer Deposition. The Al_2O_3 thin film deposition was performed using a commercial Beneq TSF200 research ALD reactor. The precursors used were trimethyl aluminum (TMA) and water, using a deposition temperature of 200 °C and a deposition rate of 1.2 Å/cycle. The resultant film thickness was measured using *in situ* ellipsometry and was targeted to be 1.5, 3, or 6 nm. The Al_2O_3 ALD is referred to in this paper as 1.5, 3, or 6 nm ALD.

2.3. Atomic Force Microscopy. The AFM is a Bruker Dimension Icon housed in a glovebox (Innovative Technologies) with an O₂ and H₂O concentration both <1 ppm. The 3-electrode (Li/Li⁺ counter and reference electrodes) electrochemical cell is a custom design by Bruker intended to interface with a Viton boot to effectively seal the cell during operation and prevent evaporation of volatile electrolyte components. The AFM was operated in peak force tapping mode with ScanAssyst Fluid tips (Bruker).

The c-AFM experiments used a PeakForce TUNA module. In the c-AFM method the sample is biased to a set voltage and as the AFM tip makes contact with the sample a current will flow through the sample and tip if the sample is conductive. Imaging of the full pit used a 500 mV bias to prevent damage to the tip on the highly conductive Ni surface. The a-Si region was imaged using a 7.5 V bias. In both cases,

platinum-coated tips were used. All AFM image processing was done with Gwyddion 2.41.³⁵

2.4. SEM. A Zeiss Auriga was used for imaging. For images prior to etching SEI with H₂O, the samples were exposed to ambient air for less than 15 s prior to pumping down under vacuum.

2.5. Electrochemistry. A CH Instruments 760D was used in galvanostatic mode at 20 μA with cutoffs of 2 V and 10 mV during cycling. A constant current hold was not performed at the cutoff voltages. The cell is a 3 electrode cell with Li/Li⁺ counter and reference electrodes and either the Si pits or pillars chip serving as the working electrode. A constant current charge and discharge of 20 μA , corresponding to an approximately 1 C rate is used to cycle the samples a total of 10 times. The 1 C rate was chosen to keep the total experiment time to about 1 day since maintaining the integrity of the AFM tip for much longer becomes challenging as a result of constant imaging. A total volume of ~600 μL of electrolyte is used in the cell. The electrolytes used are either 3:7 EC:EMC with 1.2 M LiPF₆ (referred to as “G2”) or FEC with 10 wt % LiPF₆ (referred to as “pure FEC”), or G2 with 2 wt % FEC additive (referred to as “G2 with 2% FEC”).

2.6. XPS. A Physical Electronics Instruments (PHI) VersaProbe II was used with a large area X-ray beam (200 × 1400 μm) operated at 100 W. Charge neutralization was accomplished using an 8 eV Argon ion beam and 1 eV electron beam.

3. RESULTS AND DISCUSSION

3.1. Sample Fabrication. Semiconfined microstructures were made using standard microfabrication techniques as detailed in Figure 1a–e. Briefly, a nickel (Ni) film 400 nm thick

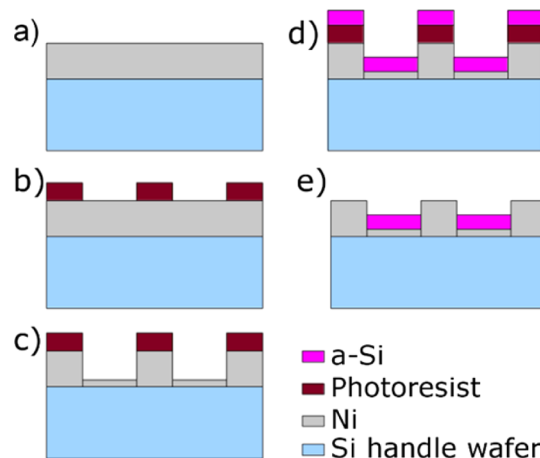


Figure 1. Fabrication flow of electrode test structures. (a) A Ni film is evaporated on the Si handle wafer. (b) Photoresist is coated and patterned on the Ni film. (c) The Ni film is ion milled. (d) a-Si is deposited into the holes created by the ion milling. (e) Lift-off is performed to remove the photoresist and a-Si film on top of the photoresist.

is evaporated on a Si handle wafer and photoresist is patterned on top of this Ni film. Using an ion milling tool, pits are etched into the Ni film in the open regions of the photoresist mask. Using electron beam evaporation, 100 nm of a-Si is deposited into the pits and the remaining photoresist is removed with a lift-off technique. For the unconfined a-Si pillars, the ion milling step is skipped.

The fabricated a-Si pits are shown in SEM images in Figure 2a and b and Raman spectra confirming the a-Si structure is shown by the broad peak near 475 cm^{-1} in Figure S1a and b. The inset in Figure 2b is an AFM image of the a-Si surface. The root-mean-square roughness of the surface is 3.29 nm. The pits

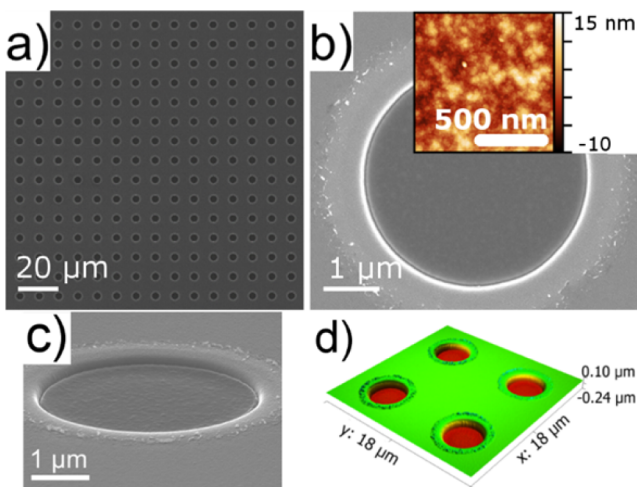


Figure 2. (a and b) SEM images of the array of a-Si pits and high magnification of a single pit, respectively. The inset in panel b is an AFM image of the surface of the a-Si. The RMS roughness is 3.29 nm. An oblique SEM image of the a-Si pit is shown in panel c along with an AFM image in panel d of a portion of the array.

have a diameter of $\sim 4 \mu\text{m}$. There is a ring of deposit around each pit, which is likely redeposition of Ni from the ion milling procedure. Figure 2c and d show an oblique SEM image of the a-Si pit and an AFM image, respectively. Additionally, the a-Si pillar structures are shown in Figure S2a and b with top down and oblique angle SEM images, respectively. Assuming a theoretical capacity of 3579 mAh g^{-1} of Li capacity for Si (Li_xSi_y), each chip that will be used in the AFM testing contains approximately $17.7 \mu\text{Ah}$ of capacity.

3.2. Electrochemical Behavior With and Without ALD.

Figure 3a and b show the electrochemical results of cycling the

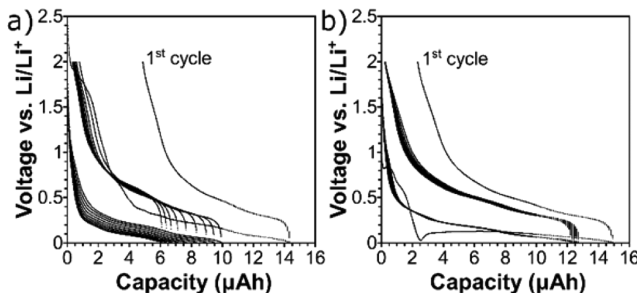


Figure 3. Voltage versus capacity plots of a-Si pit samples in G2 electrolyte (a) without ALD and (b) with 3 nm of ALD coating.

a-Si pits in G2 electrolyte without and with 3 nm of Al_2O_3 , respectively. The primary difference between the two samples occurs on the first cycle. Without ALD, the voltage profile shows a typical gradual decrease until the voltage begins to level out around 0.4 V and lithiation begins.³⁰ With ALD, the voltage rapidly decays to almost 0 V before returning to a plateau near 0.15 V. Subsequent cycles with or without ALD appear very similar. Additional results with 1.5 nm ALD in Figure S3a and b show a behavior between that of samples without ALD (Figures 3a and S2c and e) and with 3 nm of ALD (Figures 3b and S3d, f, and g). The voltage plateau near 0.4 V for the 1.5 nm of ALD is more well-defined than without ALD, but not as dramatic as with 3 nm ALD where the voltage initially drops to near 0 V.

As seen in Figure 3, the 3 nm ALD sample in the G2 electrolyte also has a slightly higher capacity on the first lithiation compared to the sample without ALD, but this could be the result of minor imperfections in the fabrication of the test samples or the relatively large volume of electrolyte used in the cell that will increase the amount of parasitic reactions caused by minor contaminants in the electrolyte. The electrochemical cycling results reveal that there is certainly an impedance from the intrinsically insulating Al_2O_3 and only with significant overvoltage does lithiation of the Al_2O_3 occur. Similarly shaped voltage versus capacity curves have been observed for Al_2O_3 coated Si.²⁶

3.3. Effect of Material Confinement and ALD Coating Thickness on Anode Performance.

Discharge capacity (lithiation) of the samples normalized to the second lithiation cycle is shown in Figure 4a for a-Si pits and pillar structures.

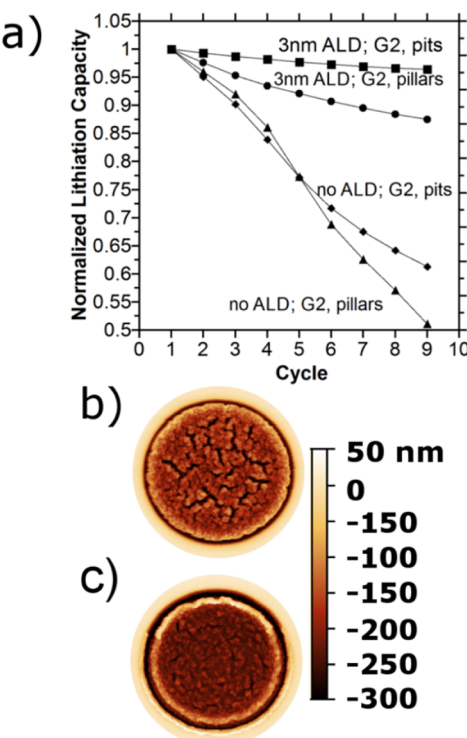


Figure 4. (a) Discharge (lithiation) capacity of a-Si pits and pillars in G2 electrolyte normalized to the second discharge. AFM images of a-Si without (b) and with (c) 3 nm of ALD and cycled in G2 taken postcycling and after rinsing the samples with deionized water.

The confined pits cycle better in both cases than the unconfined pillars. The AFM images of a-Si samples without and with 3 nm ALD cycled in G2 in Figure 4b and c, respectively, show the samples postcycling, after rinsing with deionized water to etch any SEI. Without ALD the surface is highly cracked and the diameter has not changed from the precycling state, whereas with ALD the surface is undulating but smooth and the a-Si pit diameter has actually decreased. Additionally, with 3 nm of ALD, the pit in Figure 4c is darker than the pit without ALD in Figure 4b; this indicates the pit is deeper and has recovered from the volume change better.

Furthermore, without ALD the capacity of the samples rapidly decays compared to those with ALD. This likely relates to actual mechanical damage to the a-Si structure. Figure S4b–e shows postcycling SEM images of the pillar structures and

Figure S4f and g shows in situ AFM images of the pillar after 10 cycles. It is observed that without ALD the pillar is badly cracked and damaged. The in situ AFM images of the pillar without ALD also correlate obvious thicker SEI formation to more cracking of the pillar structure relative to the 3 nm ALD pillar. With ALD, the pillar structure remains intact although there is deformation on the edge of the pillar, as the circumference of the pillar has expanded slightly and is plastically deformed. Relative to the SEM image of the as-fabricated pillar in Figures S2b and S4a, the pillar as shown in Figure S4d is still smooth and intact but has expanded after cycling. Similar behavior has been observed in smaller scale pillars without ALD and in a propylene carbonate based electrolyte.³⁰ It is interesting that the pillars have expanded in diameter after cycling, but the confined pit structures have actually decreased in diameter.

Figure 5 shows SEM images of the a-Si pits after 10 full cycles in G2 and then rinsed with deionized water to etch any

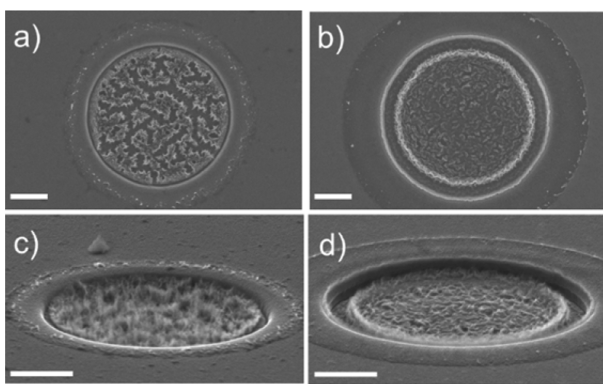


Figure 5. SEM images of a-Si pits after cycling in G2 and after rinsing with deionized water without and with 3 nm of ALD in panels a and c and panels b and d, respectively. The scale bars are 1 μm .

SEI. Additional SEM images from the pure FEC and G2 with 2% FEC electrolytes are shown in Figure S5. Without ALD in Figure 5a and Figure 5c, the pit is badly cracked and has a fuzzy structure indicating roughness. With ALD in Figure 5b and Figure 5d, the pit is still cohesive and has developed a somewhat faceted surface compared to the as-fabricated pit in Figure 2b. Also, with ALD the pit has shrunk in diameter as there is now a gap between the Ni and the a-Si. This effect has been observed in nanoconfined spaces as well.¹¹

Next, the effect of ALD thickness on the cycling performance of the a-Si anodes was investigated. Figure 6 displays the cycling results of the a-Si with either 1.5 or 3 nm ALD. In both G2 and pure FEC, the 1.5 nm coating is inferior to the 3 nm coating. The 6 nm ALD coating data is not displayed because even with a rate slowed to C/20, no lithiation was possible indicating that at that thickness the Al_2O_3 becomes completely insulating. With 6 nm of ALD, when a current is applied the sample merely polarizes and the voltage nearly immediately drops to 0 V. The in situ AFM images of the 1.5 nm pit structures in G2 and pure FEC are shown in Figure S6 and show that on the first lithiation and delithiation the a-Si remains smooth and largely recovers in volume. However, after 10 cycles, the a-Si shows a moderate permanent volume expansion and increased roughness. As will be shown in the in situ AFM images of section 3.4, the samples in Figure S6 with 1.5 nm ALD appear to resist serious damage and thick SEI growth better than

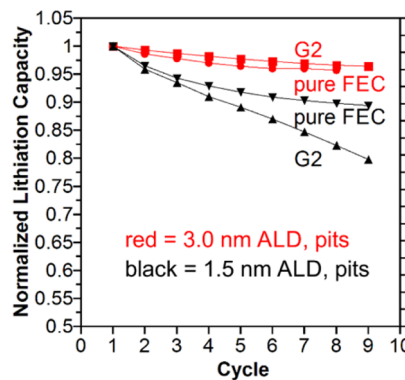


Figure 6. Discharge (lithiation) capacity of a-Si pits in G2 and pure FEC with either 3 or 1.5 nm of ALD coating.

without ALD, but the cycling data in Figure 6 reveal a capacity loss that is larger than with 3 nm of ALD.

3.4. Role of Electrolyte Composition On Performance of a-Si With 3 nm of ALD. Since the 3 nm ALD pit samples demonstrated the best electrochemical behavior relative to the 1.5 nm ALD and 6 nm ALD pits and the 3 nm ALD pillars, the remaining study on the role of electrolyte composition in cycling performance focuses on the 3 nm ALD pit samples compared to samples without ALD. Figure 7 presents the

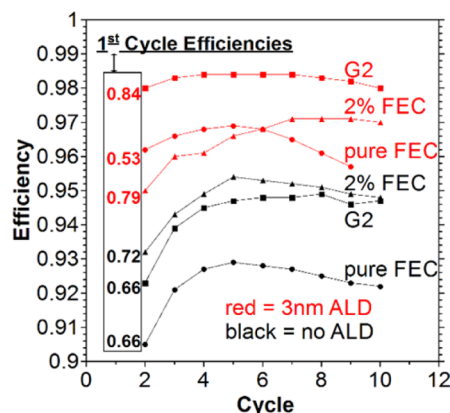


Figure 7. Cycle efficiencies of a-Si pits with (red) and without (black) 3 nm ALD in G2, pure FEC, and G2 with 2% FEC. The first cycle efficiencies are included to the left of the corresponding data for each sample.

cycling efficiency of the pits with and without 3 nm of ALD in each of the three electrolytes. The first cycle efficiencies are also shown next to the efficiency data. The efficiencies here are likely lower than would be observed in a real system as the amount of electrolyte, $\sim 600 \mu\text{L}$, used in the experiment is massive relative to the active Si material and more parasitic reactions will occur as electrolyte contaminants decompose.

Interestingly, the G2 electrolyte without any additive performs better than pure FEC or G2 with 2% FEC additive when combined with the 3 nm of ALD. This finding is intriguing as additives such as FEC and VC while typically improving Si anode performance have also been correlated to gas production during cycling, and Si cells would benefit from not requiring their use.^{36,37} The result here is unique compared to a prior study using Al_2O_3 ALD and an electrolyte with 2% VC where the VC additive enhanced capacity retention.²⁷ In addition to using VC rather than FEC, that study coated an

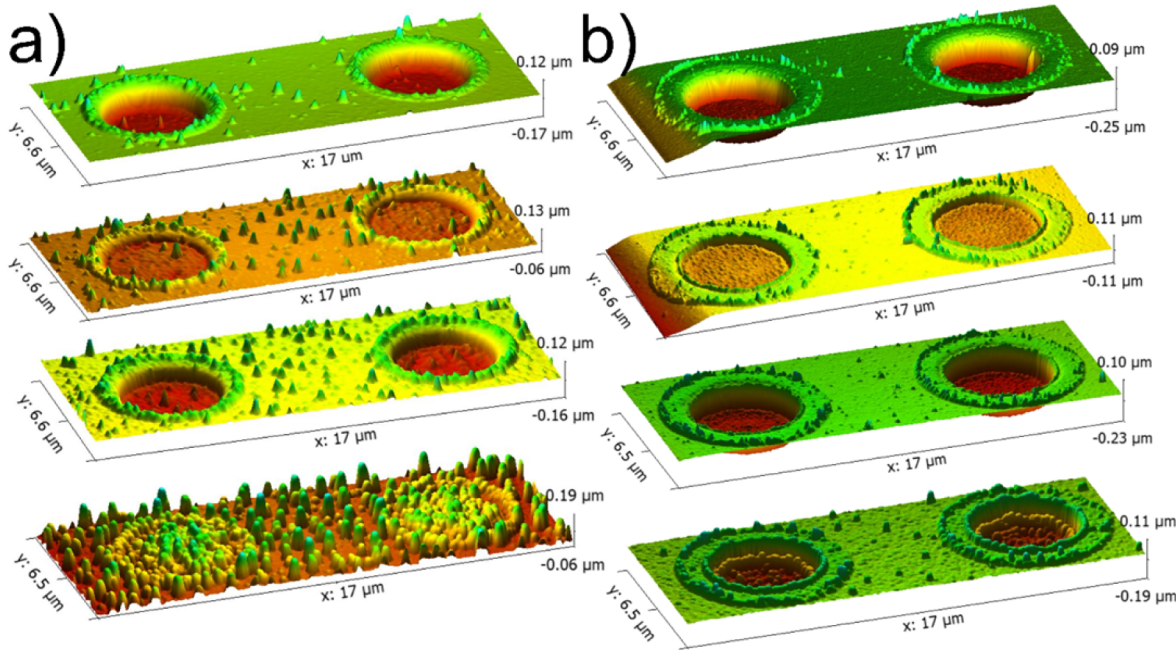


Figure 8. AFM images of a-Si pits cycled in G2 with and without 3 nm of ALD in panels a and b respectively. The top image is at OCP, the second image is the first lithiation, the third image is the first delithiation, and the bottom image is after 10 complete cycles. The sloping portion on the left side of the top two rows of panel b is an artifact of AFM imaging.

entire composite electrode, whereas this study is essentially coating individual particles. With or without ALD, the cycling efficiency in pure FEC begins to fall off after about 5 cycles.

To summarize the experiments, the actual capacities of the samples are shown in Figure S7. Because of the small quantity of material the differences in capacity may or may not be significant. As was shown in the normalized data of Figure 7 and Figure 6, the principal finding from the data in Figure S7 is that the capacity fade is much lower with 3 nm of ALD in G2 compared to 1.5 nm ALD and without ALD. Additionally, confining the a-Si into pits rather than leaving exposed as pillars helps stabilize the electrode.

The *in situ* AFM images during cycling are shown in Figure 8a and b for pits cycled in G2 without and with 3 nm of ALD, respectively. Additional AFM images of the a-Si pillars cycled in G2 and the a-Si pits cycled in pure FEC and G2 with 2% FEC are shown in Figure S8. In both Figures 8 and S8, the top images depict the samples at open circuit potential (OCP) in the electrolyte. The second row and third row of images show the pits at approximately the first full lithiation and full delithiation, respectively. The last row of images shows the samples after a full 10 cycles. Most notably, the sample with ALD develops a much thinner layer of SEI than without ALD coating. While the chemical composition is unknown, this layer is likely a true SEI layer as when the samples were immersed in H₂O to etch any residual SEI for the SEM pictures in Figure 5, the highest point of the pit is no longer above the Ni film. In other words, there is a layer of material that can be etched with H₂O as opposed to simply being a-Si that has expanded from cracking or buckling. The AFM tip develops some wear during imaging so the SEI appears as rounded growths which may not be representative of actual morphology. Nevertheless the heights of the growths are accurate. The 3 nm ALD sample can also be seen to develop a slight lip seen as a yellow band in the bottom row image of Figure 8b. This lip corresponds to the gap observed in SEM imaging in Figure 5d.

Additionally, the large amount of growth of SEI on the sample without ALD, which also develops large cracks in its structure, indicates a correlation between cracking and SEI growth. This likely results from fresh Si surface being exposed to the electrolyte as the pit cracks and thus more SEI growth develops. Also, there is significant growth on the Ni layer as has been observed in a prior study³⁰ with a propylene carbonate based electrolyte, but with ALD, the growths on the Ni are relatively minor.

The volume change of the a-Si pits is presented in Table 1. The volume is measured by recording the change in the depth

Table 1. Volume Change of the a-Si pits with and without 3 nm of ALD

		1 st Lithiation	1 st Delithiation	Final
No ALD	G2	149 ± 6	35 ± 5	285 ± 19
	G2, 2% FEC	132 ± 8	5 ± 5	104 ± 8
	FEC	129 ± 8	11 ± 10	146 ± 26
3 nm ALD	G2	180 ± 6	15 ± 5	63 ± 19
	G2, 2% FEC	160 ± 8	15 ± 5	60 ± 17
	FEC	162 ± 8	15 ± 10	84 ± 26

of the pit relative to the initial depth. The ALD coated samples actually have a slightly larger volume change in the first lithiation than samples without ALD. Since over 10 cycles the SEI formation is less, this volume increase is likely caused by increased reversible lithiation relative to samples without ALD which are growing in volume because of additional SEI growth. The FEC and G2 with 2% FEC have a larger residual volume change after the first delithiation relative to the uncoated samples, however it is minor and within experimental error. The G2 sample without ALD however has a much larger residual first cycle volume change, 35 ± 5%, versus approximately 10% for the other samples. After 10 cycles, the uncoated G2 sample has an extremely large residual volume change owing to the massive growth of SEI as seen in Figure 8.

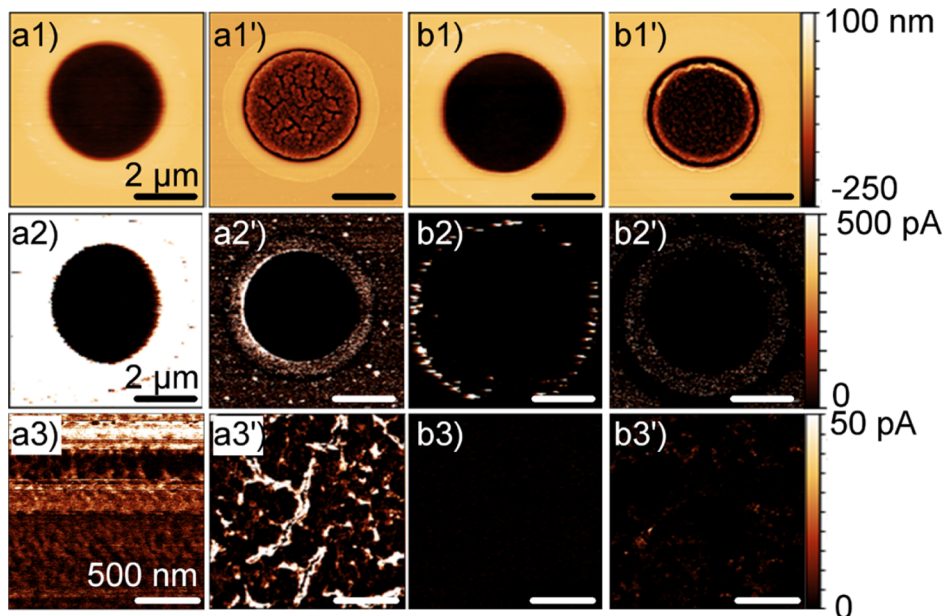


Figure 9. Topographic (top row) and conductive (bottom two rows) AFM images of a-Si pits after cycling in G2 with 2% FEC additive. The bottom row is imaged at approximately the center of the a-Si pit. Images a1–3 and a1'–3' are the pit without ALD pre and post cycling, respectively. Images b1–3 and b1'–3' are the pit with 3 nm ALD pre- and postcycling, respectively. Scale bars are consistent across rows.

The additive electrolytes decrease this SEI growth but not as much as with the ALD coating. The samples do not experience the theoretical 300% volume increase here likely because of the relatively high 1C rate, the confinement in the nickel layer, and the lack of a constant voltage hold at the end of each cycle. Prior in situ AFM work has observed the full volume change of pillar type structures, but in that study voltage control rather than current control was used.³⁰ The decreased volume change relative to the theoretical volume change is corroborated by the cycling data presented in Figure S7, where the lithiation capacity is generally less than the theoretical maximum of ~17 μ Ah. Even though the first cycle of the structures is closer to the 17 μ Ah mark, this cycle will include parasitic reactions like passivating the Ni film, breaking down any contaminants in the electrolyte, and forming an initial SEI layer.

3.5. Persistence of ALD Coating. A question remains as to whether the ALD coating is present after cycling. The results of conductive AFM (c-AFM) are shown in Figure 9 on samples without, Figure 9a1–3'), and with, Figure 9b1–3'), 3 nm ALD coatings cycled in G2 with 2% FEC electrolyte. The top row of images shows the topography of the samples; the middle row shows the c-AFM results of the pit and surrounding Ni; and the bottom row is a detailed image of the a-Si taken from approximately the center of the pit. The figures with a prime label are the postcycling images. In comparing Figure 9a2 to Figure 9b2 it is quite obvious that the 3 nm ALD coating is much more insulating and allows nearly zero current to flow except in the roughened region that exists from fabrication. As in the G2 electrolyte from Figure 8, the a-Si pit is much deeper in Figure 9a1' relative to Figure 9b1' indicating the a-Si has remained more compact and was able to better withstand the volume changes associated with lithiation and delithiation.

The c-AFM of Figure 9b3' shows that relative to the uncoated sample of Figure 9a3' the ALD coating has remained mostly intact on the sample. The sample without ALD in Figure 9a3' has significant regions of conductivity especially along cracked regions. The sample with ALD as shown in

Figure 9b3' has some conductivity compared to the precycling sample in Figure 9b3 and this conductivity seems to arise in regions where there are small cracks in the surface. A prior report using XPS and SIMS to analyze the surface of ALD coated Si electrodes postcycling in a 1 M LiPF₆ 1:1 EC:DMC electrolyte and with the SEI intact on the sample has revealed Al₂O₃ remains on the surface.²⁶ In Figure 9 the samples have been rinsed in H₂O to etch any SEI remaining prior to AFM imaging, and still an insulating layer that is likely Al₂O₃ remains.

In addition to the c-AFM results, an XPS analysis was conducted on the 3 nm ALD sample cycled in G2 electrolyte and after etching away the SEI in H₂O. The analysis does not have the lateral resolution to investigate just the Si area, but the results do show that both Al and Ni are present on the surface as thin oxides. In particular, the Ni oxide likely explains why in Figure 9a2' the current in the Ni region has been reduced relative to Figure 9a2 which has a pristine Ni film.

4. CONCLUSION

In conclusion, a-Si samples were fabricated as a semiconfined pit in Ni geometry or as pillars with the same active volume as the pits. The pits performed better than the pillar samples during initial in situ AFM tests. Additional in situ AFM tests of the a-Si pit structures in three electrolytes composed of G2, pure FEC, or G2 with 2% FEC were performed. The samples coated with 3 nm of ALD performed better in each case. Additional samples with 1.5 nm ALD did not perform as well and samples with 6 nm of ALD were too insulating to cycle at all. Surprisingly, the sample with the baseline G2 electrolyte performed even better than the two FEC based samples in electrochemical cycling studies. The samples with 3 nm ALD also grew a thinner layer of SEI relative to the samples without ALD. The postcycling analysis of the samples reveals that 3 nm ALD coated pits are mostly cohesive and have even shrunk somewhat in diameter. The samples without ALD are cracked and material has eroded from the bulk. The pillar structures with 3 nm of ALD and cycled in G2 remained intact but

suffered from a plastic deformation and expansion along the circumference of the pillar. Without ALD, the pillar structures cracked dramatically. Finally, c-AFM analysis indicates that the ALD film is still present on the pit structures after cycling despite the large changes in volume. This work along with past studies shows the potential benefits of ALD in Li-ion battery cycling. Future work will need to conclusively determine if coating individual particles or entire composite electrodes improves performance and how to practically implement ALD as part of full cell assembly.

■ ASSOCIATED CONTENT

Supporting Information

The Supporting Information is available free of charge on the ACS Publications website at DOI: [10.1021/acsami.5b09544](https://doi.org/10.1021/acsami.5b09544).

Additional Raman spectroscopy, SEM, AFM, and electrochemical cycling data ([PDF](#))

■ AUTHOR INFORMATION

Corresponding Author

*E-mail: Collin.r.becker.civ@mail.mil.

Notes

The authors declare no competing financial interest.

■ ACKNOWLEDGMENTS

We are grateful for financial support from the US Army Research Lab and Nanoscience Institute at the US Naval Research Lab. We thank John Moulder from PHI for the XPS measurements and Sam Delp from the US Army Research Lab for providing electrolytes.

■ REFERENCES

- (1) Tarascon, J. M.; Armand, M. Issues and Challenges Facing Rechargeable Lithium Batteries. *Nature* **2001**, *414* (6861), 359–367.
- (2) Beaulieu, L. Y.; Beattie, S. D.; Hatchard, T. D.; Dahn, J. R. The Electrochemical Reaction of Lithium with Tin Studied by In Situ AFM. *J. Electrochem. Soc.* **2003**, *150* (4), A419–A424.
- (3) Chan, C. K.; Peng, H.; Liu, G.; McIlwrath, K.; Zhang, X. F.; Huggins, R. A.; Cui, Y. High-Performance Lithium Battery Anodes Using Silicon Nanowires. *Nat. Nanotechnol.* **2008**, *3* (1), 31–35.
- (4) Beaulieu, L. Y.; Eberman, K. W.; Turner, R. L.; Krause, L. J.; Dahn, J. R. Colossal Reversible Volume Changes in Lithium Alloys. *Electrochem. Solid-State Lett.* **2001**, *4* (9), A137–A140.
- (5) Kasavajjula, U.; Wang, C.; Appleby, A. J. Nano- and Bulk-Silicon-Based Insertion Anodes for Lithium-Ion Secondary Cells. *J. Power Sources* **2007**, *163* (2), 1003–1039.
- (6) Baggetto, L.; Notten, P. H. L. Lithium-Ion (De)Insertion Reaction of Germanium Thin-Film Electrodes: An Electrochemical and In Situ XRD Study. *J. Electrochem. Soc.* **2009**, *156* (3), A169–A175.
- (7) Graetz, J.; Ahn, C. C.; Yazami, R.; Fultz, B. Nanocrystalline and Thin Film Germanium Electrodes with High Lithium Capacity and High Rate Capabilities. *J. Electrochem. Soc.* **2004**, *151* (5), A698–A702.
- (8) Bogart, T. D.; Chockla, A. M.; Korgel, B. A. High Capacity Lithium Ion Battery Anodes of Silicon and Germanium. *Curr. Opin. Chem. Eng.* **2013**, *2* (3), 286–293.
- (9) Chen, L.; Wang, K.; Xie, X.; Xie, J. Effect of Vinylene Carbonate (VC) as Electrolyte Additive on Electrochemical Performance of Si Film Anode for Lithium Ion Batteries. *J. Power Sources* **2007**, *174* (2), 538–543.
- (10) Dalavi, S.; Guduru, P.; Lucht, B. L. Performance Enhancing Electrolyte Additives for Lithium Ion Batteries with Silicon Anodes. *J. Electrochem. Soc.* **2012**, *159* (5), A642–A646.
- (11) Hertzberg, B.; Alexeev, A.; Yushin, G. Deformations in Si–Li Anodes Upon Electrochemical Alloying in Nano-Confining Space. *J. Am. Chem. Soc.* **2010**, *132* (25), 8548–8549.
- (12) Luo, L.; Zhao, P.; Yang, H.; Liu, B.; Zhang, J.-G.; Cui, Y.; Yu, G.; Zhang, S.; Wang, C.-M. Surface Coating Constraint Induced Self-Discharging of Silicon Nanoparticles as Anodes for Lithium Ion Batteries. *Nano Lett.* **2015**, *15* (10), 7016–7022.
- (13) Luo, L.; Yang, H.; Yan, P.; Travis, J. J.; Lee, Y.; Liu, N.; Molina Piper, D.; Lee, S.-H.; Zhao, P.; George, S. M.; Zhang, J.-G.; Cui, Y.; Zhang, S.; Ban, C.; Wang, C.-M. Surface-Coating Regulated Lithiation Kinetics and Degradation in Silicon Nanowires for Lithium Ion Battery. *ACS Nano* **2015**, *9* (5), 5559–5566.
- (14) Johnson, R. W.; Hultqvist, A.; Bent, S. F. A Brief Review of Atomic Layer Deposition: From Fundamentals to Applications. *Mater. Today* **2014**, *17* (5), 236–246.
- (15) Ferguson, J. D.; Buechler, K. J.; Weimer, A. W.; George, S. M. SnO₂ Atomic Layer Deposition on ZrO₂ and Al Nanoparticles: Pathway to Enhanced Thermite Materials. *Powder Technol.* **2005**, *156* (2–3), 154–163.
- (16) Mackus, A. J. M.; Bol, A. A.; Kessels, W. M. M. The Use of Atomic Layer Deposition in Advanced Nanopatterning. *Nanoscale* **2014**, *6* (19), 10941–10960.
- (17) Smith, G. L.; Rudy, R. Q.; Polcawich, R. G.; DeVoe, D. L. Integrated Thin-Film Piezoelectric Traveling Wave Ultrasonic Motors. *Sens. Actuators, A* **2012**, *188*, 305–311.
- (18) Marin, E.; Lanzutti, A.; Paussa, L.; Guzman, L.; Fedrizzi, L. Long Term Performance of Atomic Layer Deposition Coatings for Corrosion Protection of Stainless Steel. *Mater. Corros.* **2015**, *66* (9), 907–914.
- (19) Narayan, R.; Monteiro-Riviere, N.; Brigmon, R.; Pellin, M.; Elam, J. Atomic Layer Deposition of TiO₂ Thin Films on Nanoporous Alumina Templates: Medical Applications. *JOM* **2009**, *61* (6), 12–16.
- (20) Wang, L.; Travis, J. J.; Cavanagh, A. S.; Liu, X.; Koenig, S. P.; Huang, P. Y.; George, S. M.; Bunch, J. S. Ultrathin Oxide Films by Atomic Layer Deposition on Graphene. *Nano Lett.* **2012**, *12* (7), 3706–3710.
- (21) Piper, D. M.; Travis, J. J.; Young, M.; Son, S.-B.; Kim, S. C.; Oh, K. H.; George, S. M.; Ban, C.; Lee, S.-H. Reversible High-Capacity Si Nanocomposite Anodes for Lithium-Ion Batteries Enabled by Molecular Layer Deposition. *Adv. Mater.* **2014**, *26* (10), 1596–1601.
- (22) Kim, J. W.; Kim, D. H.; Oh, D. Y.; Lee, H.; Kim, J. H.; Lee, J. H.; Jung, Y. S. Surface Chemistry of LiNi_{0.5}Mn_{1.5}O₄ Particles Coated by Al₂O₃ Using Atomic Layer Deposition for Lithium-Ion Batteries. *J. Power Sources* **2015**, *274*, 1254–1262.
- (23) Wang, X.; Yushin, G. Chemical Vapor Deposition and Atomic Layer Deposition for Advanced Lithium Ion Batteries and Supercapacitors. *Energy Environ. Sci.* **2015**, *8* (7), 1889–1904.
- (24) Li, J.; Xiao, X.; Cheng, Y.-T.; Verbrugge, M. W. Atomic Layered Coating Enabling Ultrafast Surface Kinetics at Silicon Electrodes in Lithium Ion Batteries. *J. Phys. Chem. Lett.* **2013**, *4* (20), 3387–3391.
- (25) He, Y.; Yu, X.; Wang, Y.; Li, H.; Huang, X. Alumina-Coated Patterned Amorphous Silicon as the Anode for a Lithium-Ion Battery with High Coulombic Efficiency. *Adv. Mater.* **2011**, *23* (42), 4938–4941.
- (26) Xiao, X.; Lu, P.; Ahn, D. Ultrathin Multifunctional Oxide Coatings for Lithium Ion Batteries. *Adv. Mater.* **2011**, *23* (34), 3911–3915.
- (27) Hy, S.; Chen, Y.-H.; Cheng, H.-M.; Pan, C.-J.; Cheng, J.-H.; Rick, J.; Hwang, B.-J. Stabilizing Nanosized Si Anodes with the Synergetic Usage of Atomic Layer Deposition and Electrolyte Additives for Li-Ion Batteries. *ACS Appl. Mater. Interfaces* **2015**, *7* (25), 13801–13807.
- (28) He, Y.; Piper, D. M.; Gu, M.; Travis, J. J.; George, S. M.; Lee, S.-H.; Genc, A.; Pullan, L.; Liu, J.; Mao, S. X.; Zhang, J.-G.; Ban, C.; Wang, C. In Situ Transmission Electron Microscopy Probing of Native Oxide and Artificial Layers on Silicon Nanoparticles for Lithium Ion Batteries. *ACS Nano* **2014**, *8* (11), 11816–11823.
- (29) Liu, Y.; Hudak, N. S.; Huber, D. L.; Limmer, S. J.; Sullivan, J. P.; Huang, J. Y. In Situ Transmission Electron Microscopy Observation of

Pulverization of Aluminum Nanowires and Evolution of the Thin Surface Al_2O_3 Layers during Lithiation–Delithiation Cycles. *Nano Lett.* **2011**, *11* (10), 4188–4194.

(30) Becker, C. R.; Strawhecker, K. E.; McAllister, Q. P.; Lundgren, C. A. In Situ Atomic Force Microscopy of Lithiation and Delithiation of Silicon Nanostructures for Lithium Ion Batteries. *ACS Nano* **2013**, *7* (10), 9173–9182.

(31) McAllister, Q. P.; Strawhecker, K. E.; Becker, C. R.; Lundgren, C. A. In Situ Atomic Force Microscopy Nanoindentation of Lithiated Silicon Nanopillars for Lithium Ion Batteries. *J. Power Sources* **2014**, *257*, 380–387.

(32) Tokranov, A.; Sheldon, B. W.; Li, C.; Minne, S.; Xiao, X. In Situ Atomic Force Microscopy Study of Initial Solid Electrolyte Interphase Formation on Silicon Electrodes for Li-Ion Batteries. *ACS Appl. Mater. Interfaces* **2014**, *6* (9), 6672–6686.

(33) Hatchard, T. D.; Dahn, J. R. In Situ XRD and Electrochemical Study of the Reaction of Lithium with Amorphous Silicon. *J. Electrochem. Soc.* **2004**, *151* (6), A838–A842.

(34) McDowell, M. T.; Lee, S. W.; Harris, J. T.; Korgel, B. A.; Wang, C.; Nix, W. D.; Cui, Y. In Situ TEM of Two-Phase Lithiation of Amorphous Silicon Nanospheres. *Nano Lett.* **2013**, *13* (2), 758–764.

(35) Nečas, D.; Klapetek, P. Gwyddion: An Open-Source Software for SPM Data Analysis. *Open Phys.* **2012**, *10* (1), 181–188.

(36) Self, J.; Aiken, C. P.; Petibon, R.; Dahn, J. R. Survey of Gas Expansion in Li-Ion NMC Pouch Cells. *J. Electrochem. Soc.* **2015**, *162* (6), A796–A802.

(37) Wang, D. Y.; Sinha, N. N.; Burns, J. C.; Aiken, C. P.; Petibon, R.; Dahn, J. R. A Comparative Study of Vinylene Carbonate and Fluoroethylene Carbonate Additives for LiCoO_2 /Graphite Pouch Cells. *J. Electrochem. Soc.* **2014**, *161* (4), A467–A472.